Thiolate Spin Population of Type I Copper in Azurin Derived from [33]S Hyperfine Coupling

Marie Ramirez Cohen,[†] Netanel Mendelman,[†] Marina Radoul,[†] Tiffany D. Wilson,[‡] Masha G. Savelieff,[‡] Herbert Zimmermann,[§] Ilia Kaminker,[†] Akiva Feintuch,[†] Yi Lu,[‡][iD] and Daniella Goldfarb*,[†][iD]

[†]Department of Chemical Physics, Weizmann Institute of Science, Rehovot 76100, Israel
[‡]Department of Chemistry, University of Illinois, Urbana, Illinois 61801, United States
[§]Abteilung Biophysik, Max Planck-Institut für Medizinische Forschung, Heidelberg 69120, Germany

Ⓢ *Supporting Information*

ABSTRACT: The electron transfer mediating properties of type I copper proteins stem from the intricate ligand coordination sphere of the Cu ion in their active site. These redox properties are in part due to unusual cysteine thiol coordination, which forms a highly covalent copper–sulfur (Cu–S) bond. The structure and electronic properties of type I copper have been the subject of many experimental and theoretical studies. The measurement of spin delocalization of the Cu(II) unpaired electron to neighboring ligands provides an elegant experimental way to probe the fine details of the electronic structure of type I copper. To date, the crucial parameter of electron delocalization to the sulfur atom of the cysteine ligand has not been directly determined experimentally. We have prepared [33]S-enriched azurin and carried out W-band (95 GHz) electron paramagnetic resonance (EPR) and electron–electron double resonance detected NMR (EDNMR) measurements and, for the first time, recorded the [33]S nuclear frequencies, from which the hyperfine coupling and the spin population on the sulfur of the thiolate ligand were derived. The overlapping [33]S and ^{14}N EDNMR signals were resolved using a recently introduced two-dimensional correlation technique, 2D-EDNMR. The [33]S hyperfine tensor was determined by simulations of the EDNMR spectra using [33]S hyperfine and quadrupolar tensors predicted by QM/MM DFT calculations as starting points for a manual spectral fit procedure. To reach a reasonable agreement with the experimental spectra, the [33]S hyperfine principal value, A_z, and one of the corresponding Euler angles had to be modified. The final values obtained gave an experimentally determined sulfur spin population of 29.8 ± 0.7%, significantly improving the wide range of 29–62% reported in the literature. Our direct, experimentally derived value now provides an important constraint for further theoretical work aimed at unravelling the unique electronic properties of this site.
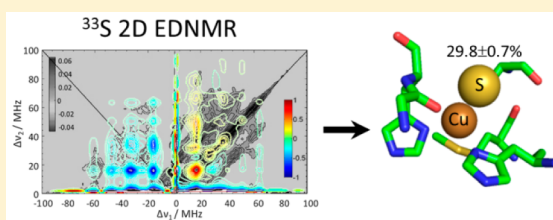
INTRODUCTION

Type I copper proteins are well-known for their involvement in electron transfer (ET) during redox reactions in biological systems. They have a unique Cu(II) site referred to as type I copper, which has been subjected to thorough structural, spectroscopic, and kinetics studies.[1−7] These unique properties are determined by specific coordination shells of the copper ion, which usually exhibit a coordination geometry ranging from trigonal bipyramidal to pseudotetrahedral.[1,8,9] The signature feature of type I copper is its characteristic ligand arrangement around the copper ion, which consists of two histidine nitrogen atoms, a cysteine thiolate ligand (Figure 1), and weaker axial ancillary ligands such as a methionine thioether or a glutamine amide on one side (top) or a glycine backbone carbonyl on the other side (bottom). In addition, it was shown that an outer-sphere hydrogen-bonding network between backbone amides and the cysteine sulfur is largely responsible for the low ET reorganization energies that characterize these proteins.[8,9] The well-known blue color of type I copper proteins results from an intense absorption band

near 16000 cm^{−1} owing to a ligand-to-metal charge transfer (LMCT) transition.[3,10] The orbitals involved in the transition are π-bonding and π-antibonding combinations of sulfur 3p and Cu 3d$_{x^2−y^2}$. The π-antibonding combination is singly occupied in the electronic ground state, and π covalency is extensive, owing to an overlap between the energetically well matched thiolate and copper d orbitals.[11,12]

It has been reported that the large variation in the redox potential among type I copper sites in different proteins with equivalent first coordination spheres is a consequence of second-sphere interactions that can be tuned by the protein structure.[13,14] These interactions comprise covalent and nonlocal electrostatic components, the former affecting the degree of covalency of the Cu–S bond[13] and, consequently, the electron delocalization on the sulfur. Therefore, the experimental determination of the Cu and S electron delocalization is

A
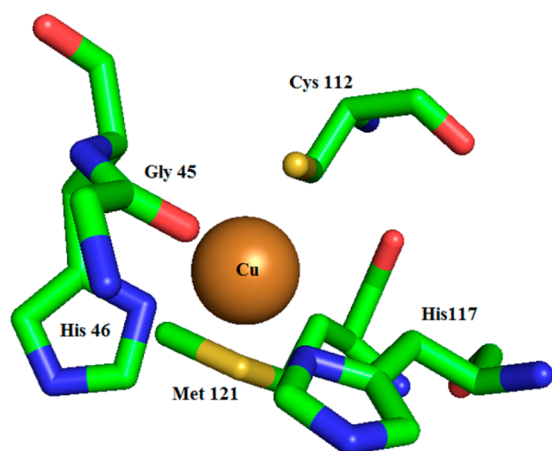
Figure 1. Trigonal-bipyramidal structure of the Cu(II) site of azurin (PDB ID: 4AZU).[23]

important, since it is closely related to the site's electronic structure and function.

A direct experimental way to probe subtle details of electronic structure is by measuring the hyperfine interaction of the unpaired electron to the copper nucleus and the neighboring ligand's nuclei. For example, the exceptionally strong electronic coupling between the protein and the metal center[15] in type I copper results in characteristic as well as a remarkably small ^{63,65}Cu hyperfine coupling ($60 < A_z < 285$ MHz),[11,12,16] ascribed to extensive spin delocalization over the ligands, particularly the thiolate sulfur. The hyperfine interaction with the thiolate sulfur has never been measured directly, but it was inferred from indirect measurements of the hyperfine coupling of the cysteine β protons by EPR[17] or paramagnetic NMR[14,18] and by S K-edge X-ray absorption spectroscopy.[11–13,19] In addition, quantum chemical calculations, which were independent or were coupled to the above experimental work, were used to calculate the spin density over the sulfur, mainly in azurin.[6,13,14,17,20–22] All of these calculations yielded sulfur spin populations in the range of 29−62% for azurin.

The absence of direct experimental data on the sulfur hyperfine interaction stems from the difficulty in preparing ^{33}S-enriched samples and because ^{33}S, as a low-γ quadrupolar nucleus, is not a "friendly" nucleus for hyperfine spectroscopic measurements. Nonetheless, there have been a few ^{33}S electron spin echo envelope modulation (ESEEM) and electron−electron double resonance (ENDOR) reports on biological systems.[24–27] Recently, it been shown that electron−electron double resonance (ELDOR) detected NMR (EDNMR)[28] is a particularly effective method, when it is applied at a high frequency such as the W band (95 GHz), for measuring nuclear frequencies of quadrupolar low-γ nuclei. It has been applied to measure ^{14}N,[29−34] ^{17}O,[35−39] ^{61}Ni,[40] ^{55}Mn,[41] ^{51}V,[42] and ^{35,37}Cl[43] nuclear frequencies, and recent reports have shown that it can also be highly useful for $I = 1/2$ nuclei such as ^{31}P.[44]

The objective of the present work was to experimentally determine the electron spin population on the thiolate ligand of type I copper in azurin via direct measurement of the ^{33}S hyperfine interaction using W-band EDNMR. To date, quantum chemical calculations have reported very large ranges of ^{33}S spin populations and were found to strongly depend on the method and functional used.[13,14,20,21] Therefore, such an experimental result should provide an additional important

constraint for calculating the electronic structure of type I copper, which is essential for understanding its unique function as an electron-transfer mediator in proteins.

We found that, while the X-band echo-detected EPR spectrum of the ^{33}S labeled azurin showed clear broadening in comparison to the spectrum of the natural abundance azurin, this broadening did not allow the detailed determination of the ^{33}S hyperfine tensor. Moreover, the ^{33}S signals, though detected in W-band 1D EDNMR spectra, were not sufficiently resolved due to a severe overlap with the ^{14}N signals of the histidine ligands even at 3.3 T. Accordingly, a recently introduced two-dimensional correlation technique (2D EDNMR[45]) was employed and allowed us to resolve the ^{33}S signal from the ^{14}N signals. In the analysis of the 1D and 2D EDNMR spectra we adapted an approach we used earlier, where we relied on spin Hamiltonian parameters obtained from quantum chemical calculations.[46,47] Specifically, we used recent QM/MM (quantum mechanics/molecular mechanics) DFT (density functional theory) results, which were carried out on azurin[14] and reported very good agreement with the experimental histidine ^{14}N and cysteine β-proton hyperfine couplings. While the authors did calculate the ^{33}S spin Hamiltonian parameters, they did not report them in the pubication but kindly made them available to us. These parameters were used as starting values in the spectral simulations and were then adjusted to satisfactorily reproduce the experimental spectra. The adjusted ^{33}S hyperfine tensor gave a 29.8 ± 0.7 ^{33}S spin population, in comparison with 36.3% predicted by the QM/MM DFT calculations.[14]

■ MATERIALS AND METHODS

Sample Preparation. ^{33}S-Na$_2$SO$_4$. Elemental sulfur-^{33}S (99.8%, 100 mg scale, Eurisotop) was deposited in a side arm of a modified Schlenk tube. An equivalent amount of metallic sodium was bulb-tube-distilled under high vacuum into a second side arm. Excess (10 mL) liquid ammonia was condensed (at −80 °C) into the sodium-containing side arm and 5 mL into the sulfur-containing side arm, while the Schlenk tube was still connected to the vacuum manifold. The distilled sodium dissolved while the mixture was stirred by a magnetic bar (sealed in a glass tube), resulting in a deep blue sodium−ammonia solution; it finally reacted with the sulfur−ammonia mixture by turning around the side arm. While the reaction mixture was warmed (1−2 h), the ammonia slowly evaporated and a white precipitate was deposited. Na$_2$S-^{33}S was collected and dried under vacuum at 150 °C.

The sodium sulfide was dissolved in a tiny amount of water while a 1/1 2 N NaOH/H$_2$O$_2$ (50%) mixture (6 mL) was added dropwise. After the exothermic reaction stopped, the stirred mixture was gently heated until the evolution of oxygen ceased. The solution was evaporated to dryness, and the crystalline solid Na$_2$SO$_4$-^{33}S·10H$_2$O was collected (a yield of 230 mg) and characterized by X-ray diffraction.

^{33}S-Labeled Azurin. The BL21-DE3 cells were transformed by a plasmid using a conventional heat-shock protocol. A 0.2 M solution of Na$_2$^{33}SO$_4$ was prepared by dissolving the salt in syringe-filtered sterilized water. Minimal M9 media was prepared as follows: the base was prepared by adding a 1/10 dilution of 10X M9 salts (567 mM NaH$_2$PO$_4$, 220 mM KH$_2$PO$_4$, 86 mM NaCl, 187 mM NH$_4$Cl, adjusted to pH 7.4) and a 1/1000 dilution of the labeled salt in water and finally autoclaving them. The media preparation was then completed by addition of a 1/66 volume ratio of a filtered 20% glucose solution, a 1/1000 dilution of filtered 2 M MgCl$_2$, 76 mM CaCl$_2$ and a 10 mg/mL biotin and thiamine solution. The starter culture was prepared by overnight growth of the transformed cells in LB media and was used to inoculate a 50 mL culture of M9 media for 8 h, 210 rpm, and 18 °C. The cells were then harvested by centrifuging the culture and were later resuspended in M9 media. The resuspended cells were used to

inoculate 360 mL of M9 media. The cells were grown overnight at 18 °C at 210 rpm. The culture was induced by addition of 0.25 mg/mL of dioxane-free IPTG at 18 °C, and growth continued overnight. Cells were then harvested and purification continued as previously reported.[48] Cu titration experiments were performed by stepwise addition from a 25 mM stock solution of $^{63}CuSO_4$ (0.5, 0.6, 0.7, 0.8, 0.9, 1.0, and 1.1 equiv). The holo-protein was then applied to a Q column for further purification and removal of extra Cu as described before.[49] The R/Z ratio of the 280 to 625 nm peak was 1.8 after purification. The pH of the final protein sample was 5.2. The control sample was made using the same protocol but with unlabeled salt. Denaturation−renaturation experiments were performed by dissolving the protein to a final concentration of 0.25 mM in 5 M guanidine hydrochloride, 1.3 mM DTT, and 1.2 mM $ZnCl_2$ in 50 mM ammonium acetate buffer pH 5.1. The protein was incubated at 37 °C for 15 min to denature. The denatured protein was then loaded into a syringe and was dripped with a rate of 1 mL/h into a stirred solution of 50 mM ammonium acetate buffer at pH 5.1 with 1.3 mM DTT and 1.2 mM $ZnCl_2$ to refold. The volume of the renaturation solution was set to keep the final concentration of guanidine hydrochloride below 1 M. The protein was then exchanged into 50 mM ammonium acetate buffer pH 5.1 by either dialysis or exchange using Centricon.

EPR Spectroscopy. X-band echo-detected EPR spectra were recorded on a Bruker ELEXSYS E580 spectrometer. All W-band (94.9 GHz) measurements were carried out using a home-built spectrometer.[50,51] Echo-detected EPR spectra were measured at 10 K using the two-pulse echo sequence ($\pi/2−\tau−\pi−\tau−$echo), where the echo intensity was registered as a function of the magnetic field. The $\pi/2$ and π pulse lengths were 30 and 60 ns, and $\tau = 0.3$ μs.

EDNMR is a hyperfine double resonance technique (see Figure 2a) in which a high-turning angle (HTA) pulse of frequency ν_2 is applied
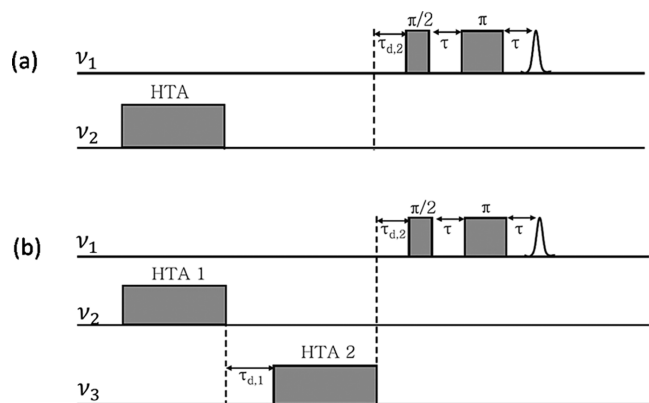
Figure 2. Pulse sequences for (a) 1D EDNMR and (b) 2D EDNMR experiments.

to a forbidden EPR transition ($\Delta m_S = \pm 1$, $\Delta m_I = \pm 1$) while the electron spin−echo intensity of an associated allowed transition ($\Delta m_S = \pm 1$, $\Delta m_I = 0$) with frequency ν_1 is observed.[28] The HTA pulse transfers the population across the forbidden transition, which reduces the population difference of the allowed transition and, therefore, the echo intensity is reduced. The EDNMR spectrum is acquired by measuring the echo intensity while sweeping the frequency, ν_2, of the HTA pulse. When ν_2 is on resonance with a forbidden transition, the frequency difference $\Delta\nu = \nu_1 - \nu_2$ matches a nuclear frequency and a decrease in the echo intensity is observed, resulting in a negative peak in the EDNMR spectrum. When $\nu_1 = \nu_2$, both frequencies are tuned with the allowed EPR transition, yielding a strong negative signal at $\Delta\nu = 0$. The EDNMR signal intensity depends on the transition probability of the forbidden EPR transitions[28] and is, therefore, particularly efficient when significant nuclear state mixing exists. This occurs when the hyperfine interaction is on the order of the nuclear Larmor frequency and/or when a significant quadrupolar interaction is present (for nuclei with $I > 1/2$). The presence of the intense $\Delta\nu = 0$

in the EDNMR experiment prevented its widespread application at conventional X-band (~0.34 T, ~9.5 GHz) frequencies, where the nuclear Larmor frequencies are low and often overlap with this signal. However, EDNMR becomes much more useful at higher microwave frequencies, where nuclear Larmor frequencies are better separated from the $\Delta\nu = 0$ signal.[29,35−37] Recently a two-dimensional (2D) EDNMR experiment has been designed (see Figure 2b) to resolve overlapping signals in the standard, one-dimensional spectrum.[43] In the 2D maps the data are displayed as a function of $\Delta\nu_1 = \nu_1 - \nu_2$ and $\Delta\nu_2 = \nu_1 - \nu_3$.

1D EDNMR measurements were performed at 10 K with the pulse sequence shown in Figure 2a. In all of the experiments the observed frequency was set to 94.9 GHz and the experimental parameters are given in Table 1. Measurements were carried out at several magnetic fields, as described in the Results and Discussion.

Table 1. 1D EDNMR Experimental Parameters

t_{HTA}, μs	$t_{\pi/2}$, ns	t_π, ns	τ, ns	$\tau_{d,2}$, μs	repetition time, ms
10	150	300	500	6	3

2D EDNMR experiments were performed using the pulse sequence shown in Figure 2b at 10 K. Because 2D EDNMR is a triple resonance technique in which the observed frequency is kept constant while two HTA pulses are swept, the configuration of our MW bridge was modified, as described in detail earlier (see the corresponding Supporting Information).[45] The experimental parameters for the 2D EDNMR experiments are given in Table 2.

The 2D spectrum was generated as described earlier.[45] The theoretical background for the simulations of the 1D and 2D EDNMR spectra are given in the Supporting Information. The 2D EDNMR simulations were performed using the experimental parameters given in Table 2 and the following parameters: electron spin spin−lattice and spin−spin relaxation times $T_{1e} = 1$ ms and $T_{2e} = 1$ μs, respectively, nuclear spin spin−lattice and spin−spin relaxation times $T_{1N} = 10$ ms and $T_{2N} = 5$ or 50 μs, respectively, for all nuclei, and $\omega_1 = 3.5$ MHz. In these simulations we took into account the orientation selectivity, which depends on both the pulse excitation bandwidth as well as the g and the ^{63,65}Cu(II) hyperfine strains. Because the 2D EDNMR calculations are very lengthy, for each field we selected the minimal selected orientation (θ, ϕ) pairs needed, 108 orientations for $B_0 = 3048$ mT and 214 for $B_0 = 3322$ mT. These were chosen by setting a threshold and selecting the most probable values while checking for convergence of the simulated spectra.

■ RESULTS AND DISCUSSION

Echo-Detected EPR Spectra. The derivatives of X-band echo-detected EPR (EDEPR) spectra of natural abundance (^{63,65}Cu) azurin, referred to as azurin, and ^{63}Cu,^{33}S-enriched azurin, referred to as ^{33}S-azurin, are shown in Figure 3a (the original spectrum, in absorption mode, is shown in Figure S1 in the Supporting Information). The spectra were recorded with a small τ value to minimize the effects of the echo decay and nuclear modulation on the EPR line shape. Both spectra resolve the typical small copper A_z value of type I Cu(II). A clear broadening is observed in the ^{33}S-azurin spectrum, particularly at the g_x, g_y region, which is attributed to the ^{33}S hyperfine splitting. The anisotropic broadening suggests that the ^{33}S hyperfine interaction is highly anisotropic. To verify that this is indeed the case, we carried out simulations of the two EDEPR spectra. The azurin spectrum was simulated using ^{63}Cu hyperfine couplings,[52] and the ^{14}N hyperfine coulings were not taken into account explicitly but rather were taken as broadening (see Figure S2a in the Supporting Information). The ^{33}S-azurin was simulated using the same parameters with the addition of the ^{33}S hyperfine interaction using the QM/MM DFT derived ^{33}S hyperfine coupling $[A_x, A_y, A_z] = [−26.96,$

Table 2. Experimental Parameters of the 2D EDNMR Measurements

sample	B_0, mT	$t_{HTA1,2}$, μs	$t_{\pi/2}$, ns	t_{π}, ns	τ, ns	$\tau_{d1,2}$, μs	repetition time, ms
azurin	3048	10	150	300	500	2	1
^{33}S-azurin	3048	5	200	400	500	5	1
^{33}S-azurin	3322	5	200	400	500	5	1
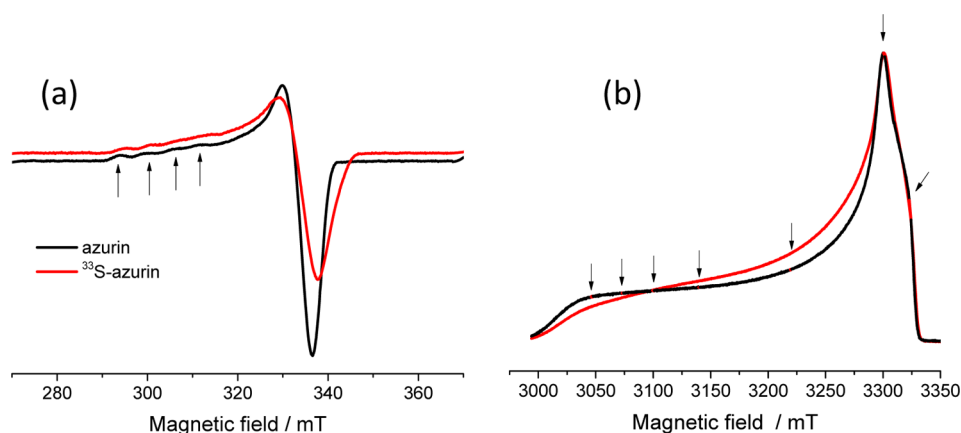
Figure 3. (a) Derivatives of the X-band EDEPR spectra of azurin (9.644 GHz) and ^{33}S-azurin (9.674 GHz), recorded at 10 K, with pulses of 16 and 32 ns and a τ interval of 120 ns. Spectra were slightly shifted vertically to allow easy comparison. The arrows indicate the resolved ^{63,65}Cu hyperfine splittings. The original spectra are shown in Figure S1 in the Supporting Information. (b) W-band echo-detected EPR spectra of azurin (black) and ^{33}S-azurin (red). The arrows indicate positions where EDNMR spectra were recorded.
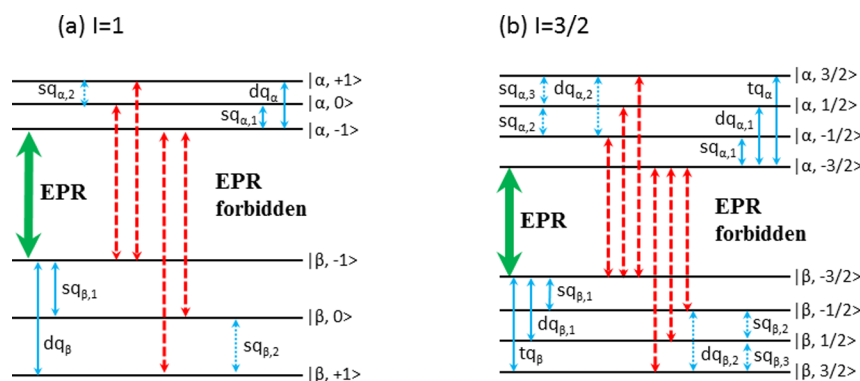
Figure 4. Energy level diagrams for $S = 1/2$ and $I = 1$ (a) and for $S = 1/2$ and $I = 3/2$ (b). Lowest energy allowed EPR transitions are highlighted in green and associated forbidden transitions in red. The NMR transitions associated with the marked allowed and forbidden transitions are shown in solid blue and all the others in dash blue.

−17.39, 89.03] MHz and the corresponding orientation of the principal axis system with respect to the g-tensor principal frame (see the Supporting Information for details). This simulation (see Figure S2b) indeed confirms that the broadening is due to the ^{33}S hyperfine interaction and that this interaction is expected to be more pronounced along g_x, g_y, because the principal direction of the hyperfine interaction is approximately perpendicular to that of g_z (see the Supporting Information). Nevertheless, as the splittings are not resolved, it does not provide an experimental confirmation for the QM/MM DFT calculated values and therefore we turned to W-band hyperfine spectroscopy methods to resolve the ^{33}S hyperfine couplings.

W-band EDEPR spectra of azurin and ^{33}S-azurin, shown in Figure 3b, do not resolve any hyperfine splitting, not even that of the ^{63,65}Cu nucleus, because of the extensive g strain. The spectrum of ^{33}S-azurin is somewhat more "smeared" at the g_z region. The presence of ^{33}S cannot account for this additional broadening, considering that its hyperfine coupling should be much smaller than that of the ^{65,63}Cu and that the broadening is expected in the $g_{x,y}$ region, as indicated by the X-band spectra. To account for this difference, we turned to simulations. Again, as for the X-band spectra, we first carried out simulations of the spectrum of the natural-abundance sample (see Figure S3a in the Supporting Information). To reproduce it, we had to add a rather large strain. Simulations of the ^{33}S-azurin spectrum, particularly the broadening at the g_z region, required increasing the strain significantly (see Figure S3b). We do not know the origin of this broadening, and we do exclude the presence of some minor impurity. To further confirm that the type I Cu(II) center in the enriched sample center has not been modified by the isotope enrichment procedure, we compared the W-band ^{1}H spectra of ^{33}S-azurin and azurin. The spectra of the two samples are identical (Figure S4 in the Supporting Information), and the large hyperfine couplings of the cysteine β protons, which are signatures of type I Cu(II), are clear in both.

In an attempt to resolve the [33]S hyperfine couplings, we carried out W-band ENDOR and X-band and W-band HYSCORE (hyperfine sublevel correlation spectroscopy) measurements on the enriched and natura-abundance samples but did not detect any differences between the two that could be attributed to the [33]S signals. All spectra were dominated by signals of the direct and remote ^{14}N nuclei of the histidine ligands and the cysteine β protons. We also did not detect the methionine [33]S, but this is not surprising, because it is expected to have a very small hyperfine coupling, as the QM/MM DFT predicts ($[A_x A_y A_z] = [-0.55, -0.91, -0.99]$ MHz), and a comparable size quadrupolar interaction (see the Supporting Information). In striking contrast, we were able to detect the [33]S signals by W-band EDNMR measurements, and these are described next.

1D EDNMR. In EDNMR spectra of natural-abundance azurin we expect to see signals due to the coordinated [14]N ($I = 1$) of the histidines. Figure 4 shows the energy level diagram for an $S = 1/2$, $I = 1$ spin system. The six energy levels are labeled as $|\alpha,+1\rangle$, $|\alpha,0\rangle$ and $|\alpha,-1\rangle$ for the upper electron manifold and $|\beta,+1\rangle$, $|\beta,0\rangle$, and $|\beta,-1\rangle$ for the lower electron manifold. In total there are four nuclear single quantum transitions (sq$_{\alpha1,2}$, sq$_{\beta1,2}$) and two nuclear double quantum transitions (dq$_\alpha$ and dq$_\beta$) that can be observed in the EDNMR spectrum. When the ^{14}N hyperfine couplings are small and are not resolved in the EPR spectrum due to excessive inhomogeneous broadening, the observed pulses are not selective with respect to the ^{14}N hyperfine coupling. Accordingly, the various allowed transitions cannot be distinguished and all contribute to the EDNMR spectrum, through different spin packets. This results in the symmetrical appearance of the EDNMR spectrum with respect to $\Delta\nu = 0$.

EDNMR spectra of azurin, shown in Figure 5, were measured at seven different magnetic field positions along the EPR powder pattern, as shown with arrows in Figure 3. The spectra are symmetrical around $\Delta\nu = 0$, and we therefore present only half of each (the complete, as-recorded spectra are presented in Figure S5 in the Supporting Information). The EDNMR spectra of azurin are dominated by the signals of the directly coordinated ^{14}N of His117 and His46. The hyperfine couplings of these ^{14}N nuclei are around 20 MHz,[53] and therefore they fulfill the "cancellation condition"[54] ($\nu_I \approx A/2$, where A is the hyperfine coupling and ν_I is the nuclear Larmor frequency, at W-band $\nu_{I(^{14}N)} \approx 10$ MHz). Under this condition, the mixing of the nuclear spin states is maximized, thus leading to an increase in the transition probability of the forbidden EPR transitions which involve, in addition to the electron spin flip, also a nuclear spin flip and consequently leading to strong peaks in the EDNMR spectra. The signals corresponding to the manifold in cancellation are usually narrow also in orientationally disordered samples because of their very weak magnetic field dependence, which practically abolishes their orientation dependence. Furthermore, they have very low frequencies and therefore in our case they overlap with the central hole.[53−56] The ^{14}N signals of the other spin manifold owing to single quantum (sq) transitions appear around 20 MHz, and weaker signals owing to the double quantum (dq) transition appear around 40 MHz. In the spectrum recorded close to the g_z position (3048 mT), the signals of the two histidines can be resolved (denoted by arrows). On the basis of earlier reports of the hyperfine coupling of these ^{14}N nuclei,[53] sq signals for ^{14}N of His46 are expected at around 19 MHz and dq signals at around 38 MHz. Frequencies associated with directly
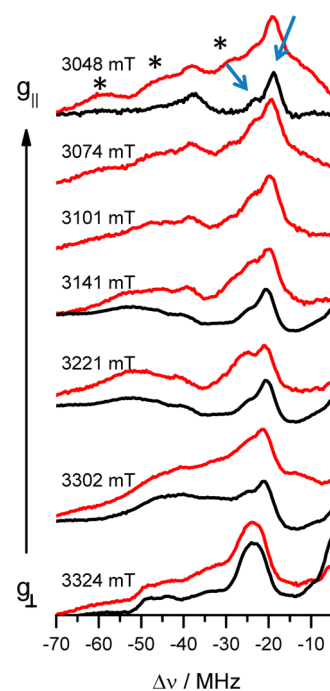
Figure 5. W-band EDNMR of azurin (black) and [33]S-azurin (red) recorded at different magnetic field positions along the EPR powder pattern, as indicated in Figure 3b. The intensities, originally negative, are displayed as positive. The central holes are not displayed. The signals denoted by arrows indicate those corresponding to the ^{14}N of the two histidines, and the asterisks denote [33]S signals.

coordinated ^{14}N of His117 are expected to be around 22−23 MHz[53] for sq transitions and at ~44−46 MHz for the dq transitions. The two lines at ~22 and 44 MHz are observed as shoulders on the more intense His46 signals at ~19 and 38 MHz, respectively. This lower signal intensity is expected, since the hyperfine coupling of this ^{14}N is farther away from the cancellation condition.

The [33]S spin system ($I = 3/2$) is more complex, and it contains eight energy levels with four allowed EPR transitions, each corresponding to a different [33]S nuclear state. Figure 4b highlights a particular allowed transition with its associated forbidden transitions. In principle, in such a spin system the nuclear transitions that can be observed in the EDNMR spectrum are six single quantum transitions, three in each electron manifold (sq$_{\alpha1,2,3}$ and sq$_{\beta1,2,3}$), two double quantum transitions in each manifold (dq$_{\alpha1,2}$ and dq$_{\beta1,2}$), and one triple quantum transition per manifold (tq$_\alpha$ and tq$_\beta$). This makes a total of 12 transitions, 6 per manifold, generating congested EDNMR spectra. EDNMR spectra of [33]S-azurin are shown in Figure 5 as red traces. [33]S signals at 30, 45, and 60 MHz are resolved only in the low-field spectra, particularly at 3048 mT (denoted by asterisks in Figure 5), and as the magnetic field position is increased toward $g_{x,y}$, they broaden. Nevertheless, signal intensities attributed to unresolved [33]S signals are present throughout the spectra measured at all magnetic field positions.

We attempted to isolate the [33]S signals by subtracting the EDNMR spectra of the azurin spectra from the spectra of [33]S-azurin, but because of uncertainties in the normalization of the spectra, the results were ambiguous. Therefore, we turned to spectral simulations of the spectra for data analysis, taking both the ^{14}N and [33]S signals into account. The approach we used is as follows: the first step was to simulate the spectra of the

Table 3. ^{63}Cu, ^{14}N Hyperfine, and Quadrupole Principal Values and Euler Angles Taken from the Literature (Row a) along with the Modified ^{14}N Hyperfine Values that Gave the Best Fit of the Simulated Spectra for the 1D Experimental Spectra (Row b)

nucleus	$[A_x,A_y,A_z]$, MHz	$[P_x,P_y,P_z]$, MHz	Euler angle (α,β,γ), A to g, deg[a]
^{63}Cu[52]	(a) [30,18,172.2]	[−2.83,−0.83,3.66]	[60,10,10]
	(b) [−30,18,178] ± 1		
^{14}N (His46)[53]	(a) [19.1,18.0,17.2]	[−0.36,−1.09,1.45]	[78.3,23.4,80.2]
	(b) [24,21,17.8] ± 0.8		
^{14}N (His 117)[53]	(a) [27.8,24.0,23.6]	[−0.25,−1.0,−0.5]	[141.5,140.6,−94.6]
	(b) [32.8,25.0,24.5] ± 1.5		

[a]The Euler angles that relate the hyperfine and quadrupole principal axis systems (taken as coinciding) relative to the principal axis system of g.

Table 4. ^{33}S Hyperfine and Quadrupole Principal Values and Euler Angles of ^{33}S Obtained from QM/MM DFT Calculations (see the Supporting Information) (Row a),[14] those Determined from the 1D Spectra Simulations (Row b) and Those Obtained from the 2D EDNMR Simulations (Row c)[a]

$[A_y,A_x,A_z]$,[b] MHz	$[P_y,P_x,P_z]$,[b] MHz	Euler angle A to M, deg	Euler angle P to M, deg	Euler angle g to M, deg
(a) [−26.96,−17.39, 89.03]	[2.97,0.26,−3.24]	[112.5,82.7,−139.2]	[5.4,65.2,133.8]	[108.3,77.9,−57.5]
(b) [−17.0,−15.4, 89.0] ± 0.6	[2.97,0.26,−3.24]	[112.5,82.7,−139.2]	[5.4,65.2,133.8]	[108.3,77.9,−57.5]
(c) [−27.0 ± 1,−15.4 ± 1,67.5 ± 2.5]	[2.97,0.26,−3.24]	[113,63 ± 2,−139]	[5.4,65.2,133.8]	[108.3,77.9,−57.5]

[a]M represents the molecular axis system used in the QM/MM DFT[14] calculations. [b]In order to extract the Euler angles from the direction cosine matrices given in the SI we needed to exchange the x and y axes to get a positive determinant.

azurin sample using the spin Hamiltonian parameters of the ^{14}N of His46 and His117 derived from single-crystal measurements[53] and account for possible ^{63,65}Cu signals also using the reported hyperfine values.[52] To reproduce the signal frequencies in the EDNMR spectra, we had to introduce minor changes in the reported ^{14}N parameters. This confirmed and assisted in the identification of the ^{33}S signals. Next, we simulated the spectra of ^{33}S-azurin, which includes contributions from ^{14}N and ^{63}Cu as well as from ^{33}S. In the simulations we used the ^{14}N and ^{63}Cu parameters derived from the simulations of the natural-abundance azurin and for the ^{33}S hyperfine and quadrupolar parameters we employed values derived from QM/MM DFT calculations[14] as starting values. The orientations of the g, ^{33}S hyperfine, and quadrupole interaction principal axes given by these calculations, with respect to the Cu(II) coordination bonds, are given in Figure S6A−C in the Supporting Information. The g_z direction forms a 14.4° angle with the Cu−S(Met121) direction, in excellent agreement with the 15° reported by a single-crystal EPR study.[57] The angle between the ^{33}S hyperfine A_z direction and Cu−S(Cys112) bond is 86°, and the quadrupole Q_z makes a 130° angle with the same bond.

When evaluating the agreement between the experimental and simulated spectra, we mostly focused on matching the frequencies and not their relative intensities, because in the simulations we did not account for all factors affecting the experimental spectra, such as cavity bandwidth and variation of the effective ω_1 (amplitude of the applied microwave irradiation) over the various transitions and its orientation dependence, since the spectra were recorded with a constant HTA pulse.

The spin Hamiltonian parameters used for the EDNMR simulation are summarized in Tables 3 and 4, and experimental parameters relevant to simulations are presented in Table S1 in the Supporting Information.
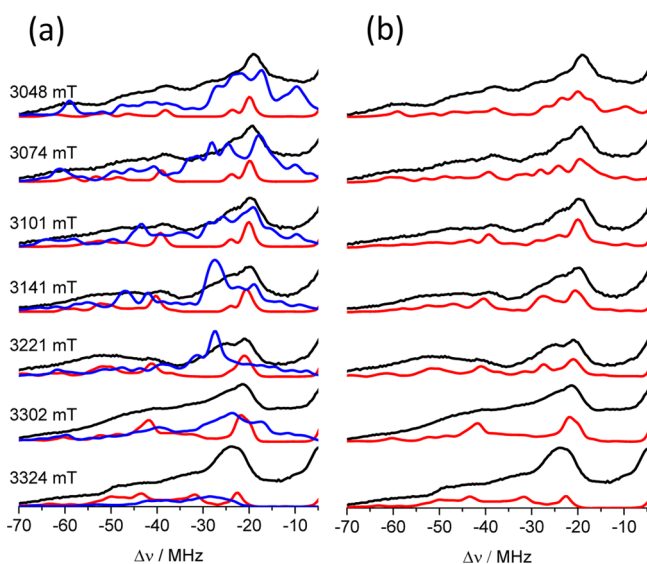
The calculated ^{14}N and ^{63}Cu EDNMR spectra of azurin using the literature parameters that are given in Table 3, in comparison with the experimental spectra (Figure S7b in the Supporting Information), revealed a small mismatch in some of the frequencies of the ^{14}N signals. To improve the fit, we varied

only the principal values of the ^{14}N hyperfine interaction until a satisfactory fit of the peak frequencies was obtained. The resulting spectra are shown in Figure S7a and the adjusted values are given in Table 3 (row b). We attribute this change to subtle differences in the structures in solution and in the crystal. For ^{63}Cu(II), the sign of A_x was changed to obtain a better fit and we attribute this to the uncertainty of simulations of the EPR spectra due to the limited resolution of the EPR spectrum in the $g_{x,y}$ region and the relatively small associated hyperfine coupling. For simplicity, we did not consider the smaller contribution of ^{65}Cu (natural abundance 30.8%).

After determining the ^{14}N and ^{63}Cu hyperfine couplings from the EDNMR spectra of azurin, we proceeded to simulate the ^{33}S-azurin spectra using the ^{33}S spin Hamiltonian parameters predicted from the QM/MM DFT calculations. This involved a total of 11 parameters: 5 for the nuclear quadrupole interaction and 6 for the hyperfine interaction. The simulations using this set of parameters are shown in Figure S8 in the Supporting Information. The main criteria we used for evaluating the fit of the ^{33}S peaks focused on the resolved peaks denoted by asterisks in Figure 5 in the spectrum recorded at 3048 mT. These peaks are also clear at 3074 mT. At higher fields the copper signals become more intense and it became harder to resolve the ^{33}S peaks. The fit obtained with the QM/MM DFT ^{33}S parameters was improved by varying only the principal hyperfine values by manual trial and error; the values obtained are given in Table 4 (row b), showing that a variation of 10 MHz for ^{33}S A_y and 2 MHz for A_x was required. Figure 6 shows the best-fit simulated spectra including all nuclei involved with the parameters given in Tables 3 and 4 (row b).

Because of the considerable overlap between the ^{33}S and ^{14}N signals in the 1D-EDNMR spectra, we turned to 2D EDNMR, hoping to better resolve the ^{33}S signals and substantiate the determination of the ^{33}S hyperfine parameters from the 1D EDNMR simulations. The measured 2D EDNMR spectra were reported earlier as an example when the 2D EDNMR technique was first reported,[45] but without any data analysis. Here we present the spectra again with analysis and simulations.

**2D EDNMR.** We first discuss the 2D EDNMR of azurin, where only ^{14}N contributes. The 2D EDNMR spectrum of

Figure 6. ^{33}S-Azurin EDNMR spectra as a function of the observer field positions: (a) black traces giving experimental spectra, red traces giving simulated spectra of azurin (^{14}N and ^{63}Cu), and blue traces giving simulated spectra of ^{33}S only, calculated using the modified hyperfine values given in Table 4, row b; (b) black traces giving experimental spectra and red traces giving simulated EDNMR spectra of ^{33}S-azurin after summing the simulated EDNMR spectra in (a).

azurin, measured around the g_z region (B_0 = 3048 mT), is presented in Figure 7a. The spectrum shows a set of negative cross peaks (blue) at (19,~0) and (38,~0) MHz, as expected from the 1D EDNMR measurements. These negative correlation peaks arise from cross peaks between NMR frequencies in different electron submanifolds.[45] They appear very close to the axis because of the low frequencies of the nuclear transitions within the electron spin manifold for which the cancelation condition holds. The position of the His117 signal is indicated by an arrow in Figure 7a. It also shows a positive peak on the diagonal at (19,19) MHz. Whereas the 1D simulations did not require taking into account the off-resonance effects of the HTA pulse and electron and nuclear relaxation, the 2D simulations did. Using the theory described in the Supporting Information,[45] the 2D EDNMR spectrum of azurin was simulated with the ^{14}N spin Hamiltonian parameters

determined from the 1D EDNMR simulations (Table 3). The result of the simulations for the sum (1:1) of the spectra of His46 and His117 is presented in Figure 7b. The simulation reproduces most of the peaks in the experimental spectra. The positive peaks on the diagonal at 20−23.0 MHz correspond to the overlap of correlations within the electron spin manifold: $sq_{\alpha1,2}$ (23.40 and 23.05 MHz) of His117 and $sq_{\alpha1'2}$ (22.10 and 19.7 MHz) of His46. The simulations are in very good agreement with the experiment.

The 2D EDNMR spectra of ^{33}S-azurin, recorded at 3048 mT ($\sim g_z$) and 3322 mT ($\sim g_x$), are displayed in Figure 8. If we consider ^{33}S alone, negative cross peaks are expected between frequencies belonging to different electron spin manifolds, and for the nonselective case (in terms of the ^{33}S hyperfine coupling in the EPR spectrum) a maximum of 36 cross peaks can appear: $9 \times (sq_{\alpha}, sq_{\beta})$, $6 \times (sq_{\beta}, dq_{\alpha})$, $6 \times (sq_{\alpha}, dq_{\beta})$, $3 \times (tq_{\alpha}, sq_{\beta})$, $3 \times (sq_{\alpha}, tq_{\beta})$, $4 \times (dq_{\alpha}, dq_{\beta})$, $2 \times (tq_{\alpha}, dq_{\beta})$, $2 \times (dq_{\alpha}, tq_{\beta})$, and $1 \times (tq_{\alpha}, tq_{\beta})$. However, cross peaks involving double (dq) and triple quantum (tq) transitions are expected to have lower transition probabilities. Therefore, with positive signals on the diagonal and positive cross peaks owing to off-resonance excitation effects for an intense HTA pulse,[30,45] the spectrum is expected to be highly congested. Indeed, the spectra shown in Figure 8 are quite congested, particularly in the (+,+) quadrant, and a comparison with the spectrum of azurin indicates that the signals come primarily from ^{33}S, particularly for the 3048 mT spectrum, which is recorded at a field position where the ^{63}Cu lines appear above 100 MHz. In the (+,+) quadrant, the signals are positive and reveal two ridges running parallel to the diagonal with a frequency separation of 44 MHz for the g_z and $\sim$50 MHz for the g_x spectrum. Within the ridges of the g_x spectrum (Figure 8a), which is expected to be more resolved, some peaks at frequencies similar to those detected in the 1D EDNMR spectra can be identified at about (60,38), (30,38), and (28,45) MHz along with their more or less symmetric counterparts. The negative signals in the (−,+) quadrant, which are however weaker, are better resolved.

The 2D EDNMR spectra were analyzed with the help of simulations. Initially we used the spin Hamiltonian parameters derived from the 1D simulations listed in Tables 3 and 4 and using the g values reported from the single-crystal EPR data[52] (see Table S1 in the Supporting Information). For the B_0 = 3048 mT spectrum, the 60 and 38 MHz signal in the (−,+)
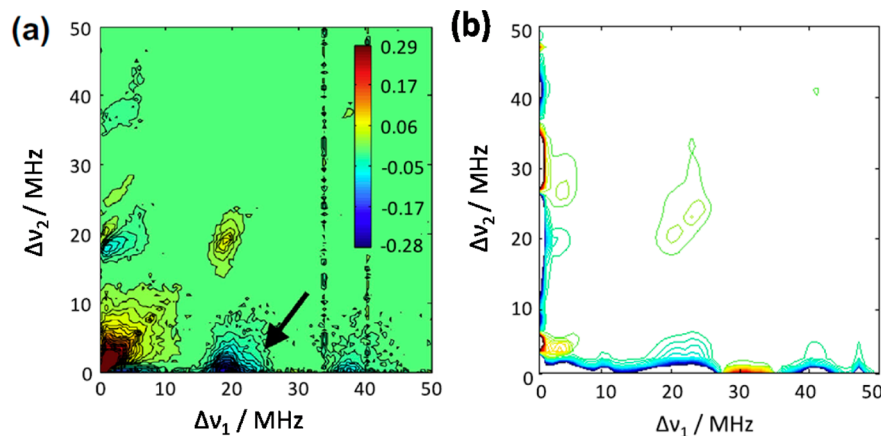

Figure 7. (a) 2D EDNMR of azurin measured at 3048 mT. (b) Right upper quadrant of simulated 2D EDNMR of His46 and His117. The parameters used in the simulation are given in Table 3, row b. Other parameters are T_{1e} = 1 ms, T_{2e} = 1 μs, T_{1N} = 10 ms, T_{2N} = 5 μs, and ω_1 = 3.5 MHz. The experimental spectrum was reproduced from ref 45.
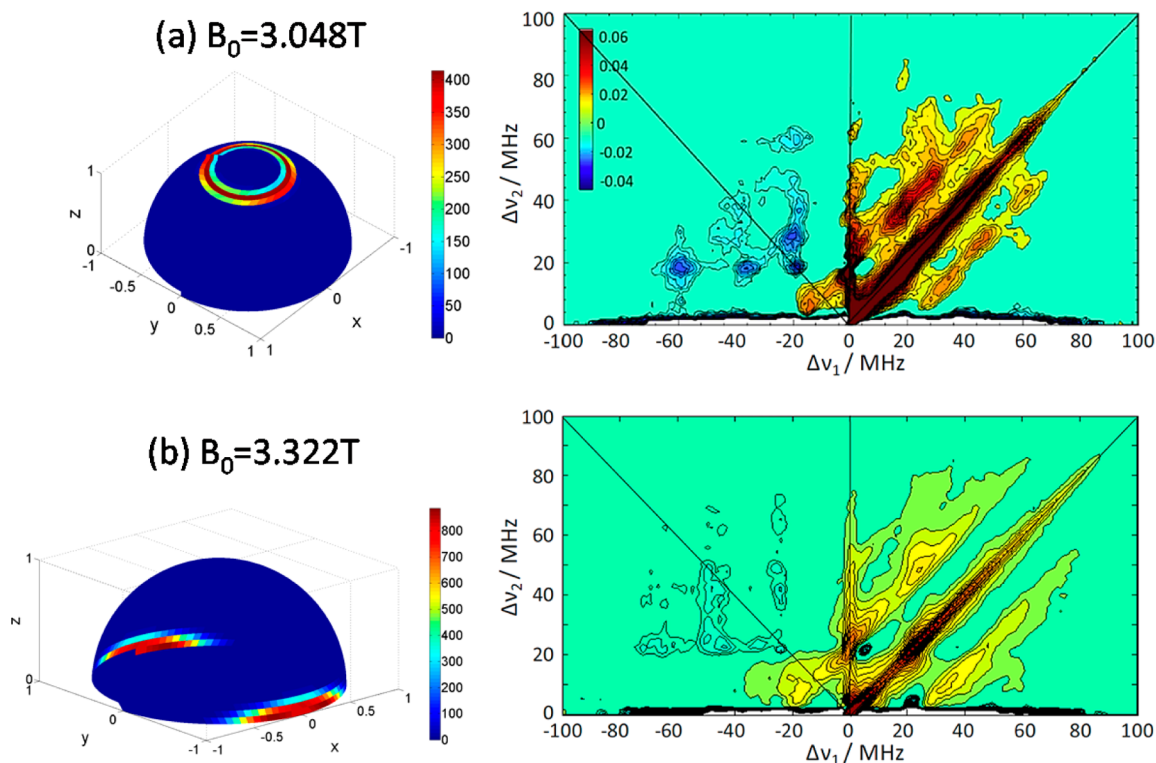
Figure 8. 2D EDNMR spectra of ^{33}S-azurin measured at (a) 3048 mT and (b) 3322 mT along with the range of B_0 orientations, relative to **g**, selected at each particular field on the left. The scale refers to the relative probability for each orientation. The spectra were reproduced from ref 45.

quadrant could not be reproduced and even larger deviations were observed for B_0 = 3322 mT, as shown in Figure S9 in the Supporting Information. The simulations also included T_{1e}, T_{1N}, T_{2e}, T_{2N}, and ω_1. Among these, T_{1N}, which is unknown, was found to affect the intensities and the width of cross peaks but not their positions; thus, by varying the T_{1N} value we could not improve the agreement. In addition, using the original QM/MM DFT parameters did not produce satisfactory fits (Figure S10 in the Supporting Information). Therefore, focusing mainly on the peak positions in the (−,+) quadrant, we proceeded by varying the ^{33}S principal hyperfine values and the β Euler angle (see Table 4). The best fit was manually achieved by reducing A_z from the QM/MM DFT predicted value of 89 MHz to 65−70 MHz and reducing β from 82.7° to 60−65°. In addition, we estimate the range of the A_x and A_y values that can fit the data values to be ±1 MHz. In Figure 9 we present the simulated spectra, obtained with the parameters listed in Table 4, row c, displayed on top of the experimental spectra. Other simulated spectra obtained using parameters within this range given above are given in Figure S11 in the Supporting Information. The simulation reproduced the congestion of the positive peaks in the (+,+) quadrant and the negative peaks in the (−,+) quadrants. They also show that most of the positive peaks (yellow color in the 2D spectra) do not have symmetric counterparts, indicating that they originate from the off-resonance excitation of allowed transitions.[45] Although the simulations reasonably reproduced the position of the peaks in the diagonal upper part of the (+,+) quadrant, the part below the diagonal was not well reproduced. This was independent of the parameters used. The spectra calculated with the same parameters as those given in Figure 9, but with a T_{1N} value of 100 μs, are quite similar to those calculated with T_{1N} = 10 ms (see Figure S12 in the Supporting Information).
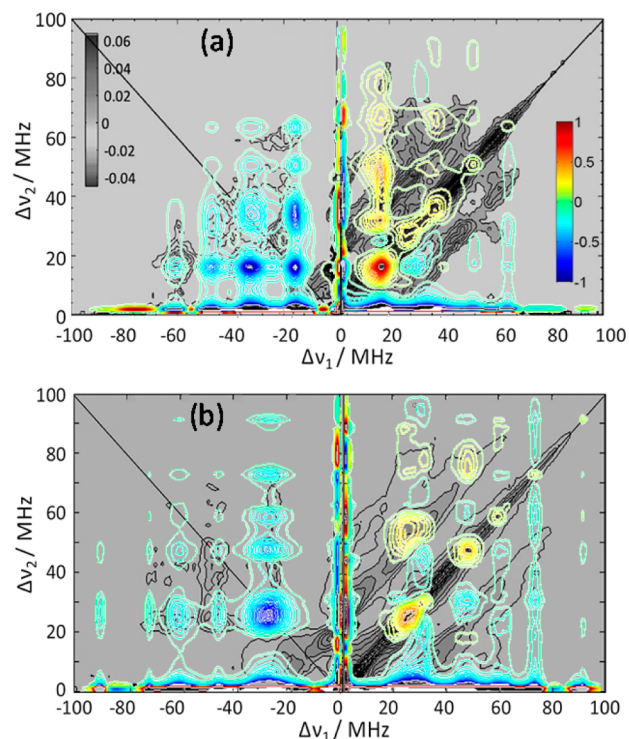
Figure 9. Simulated 2D EDNMR spectra calculated with the parameters given in Table 4, row c, with A_z = 70 MHz, β = 61°, T_{1e} = 1 ms, T_{2e} = 1 μs, T_{1N} = 10 ms, T_{2N} = 5 μs, and ω_1 = 3.5 MHz: (a) B_0 = 3048 mT; (b) B_0 = 3322 mT. The experimental spectra are presented as a gray background, whereas the simulations are shown in color.
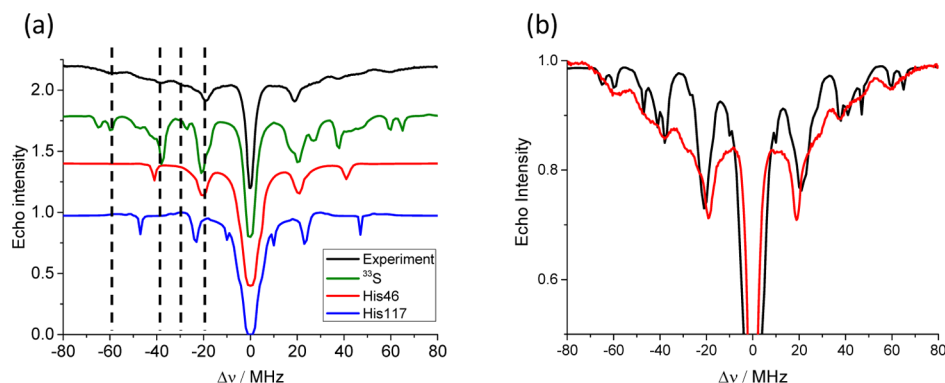
Figure 10. Simulated 1D EDNMR spectra recorded at B_0 = 3048 mT with the parameters given in Table 3, row b, and Table 4, row c (with A_z = 70 MHz and β = 61°): (a) individual spectra of each of the nuclei as denoted in the figure (dashed lines mark peak positions in the experimental spectrum for easy comparison) and (b) their sum (black trace) compared with the experimental spectrum (red trace). The spectra were calculated with ω_1 = 3.5 MHz and T_{2e} = 10 μs.

In these simulations one has to take into account the orientation selectivity, which depends on both the pulse excitation bandwidth and on **g** and the ^{63,65}Cu(II) hyperfine strains. The symmetry of the 1D spectra about $\Delta\nu$ = 0 indicated that there is no selectivity in terms of the observed allowed transition. The strain was taken into account as an increased "effective" excitation bandwidth used to determine the range of orientation selected. It was adjusted such that the calculated 1D spectrum also gave a spectrum with minimal asymmetry. We note that simulations were done under the assumption that ^{33}S is the major contributor to the 2D EDNMR spectra, thus neglecting the possibility of contributions from transitions involving two nuclei flips, ^{14}N and ^{33}S. These usually occur in the presence of strong signals of the individual nuclei and are readily identified in the 1D EDNMR spectrum.[39] We do not know how strong they should be in the 2D EDNMR spectrum.

Now that we have a set of parameters which reasonably reproduce the 2D-EDNMR spectra, we used them to recalculate the 1D spectra using the same theoretical formalism used to calculate 2D-EDNMR. In Figure 10 we present the simulations of the spectrum recorded at 3048 mT in comparison to the experimental spectrum. The line positions are reproduced rather well; however, because of an overly strong contribution of ^{14}N of His117, the line at 19 MHz is slightly shifted. The agreement between the experimental spectra using this set of parameters (Table 3, row b, and Table 4, row c) and the set used to simulate the 1D spectra using a simpler theoretical approach (Figure 6, Table 3, row b, and Table 4, row b) is of the same quality. Accordingly, we conclude that the set of hyperfine parameters derived from the 2D EDNMR spectral simulations is in better agreement with the experimental data (Table 4, row c). Calculated 1D ^{33}S EDNMR spectra showing the effect of ω_1 and T_{1e} for spectra recorded at 3048 mT are presented in Figure S13 in the Supporting Information.

The implications of the change in the β angle from 82.7° to 60−65° (see Table 4) in terms of the orientation of the principal axis system of the ^{33}S hyperfine interaction with respect to the structure of the type I site are given in Figure S4 in the Supporting Information. While the A_z direction did not change much and it makes an angle of 77° with respect to Cu−S(Cys112), in comparison to 86° for QM/MM DFT values, the A_x and A_y axes have rotated. The orientation of the A_z direction is expected, considering that the Cu−S(Cys112)

bonding involves π-bonding and π-antibonding orbitals which are combinations of Sulfur 3p and Cu 3d$_{x^2-y^2}$ and not the corresponding σ components along the bond axis. The π-antibonding combination is the singly occupied orbital, and therefore the orientation of A_z is expected to be approximately perpendicular to the Cu−S direction.[6]

Finally, we recalculated the X-band EPR spectrum with the new ^{33}S hyperfine tensor (principal component and orientation) and compared it with the experimental spectra (see Figure 4c) and we observe a slight improvement in term of intensities in the $g_{x,y}$ region.

Calculations of the ^{33}S Spin Population. Now that we have determined the ^{33}S hyperfine coupling parameters, we can proceed and derive from them the ^{33}S spin population. This was achieved using the tables of Morton and Preston,[58] which give the calculated isotropic hyperfine value, A_{iso}, and the anisotropic hyperfine value, $T_\perp$ (average of T_x and T_y), arising from one unpaired electron in the 3s and 3p orbitals of ^{33}S. Taking into account the angular factor for the p orbitals (x,y,z), the principal components of **T** ($-T_\perp,-T_\perp,2T_\perp$) for the ^{33}S 3p orbitals become ($-2/5,-2/5,4/5$) × 251.3 MHz. For a unit spin in the 3s orbital of ^{33}S the tables give an isotropic hyperfine coupling of 3463 MHz. The range of the principal values that gave reasonable agreement with the experimental 2D spectra were ($-27.0 \pm 1,-15.4 \pm 1,67.5 \pm 2.5$) MHz; these yield A_{iso} = 6.9−9.9 MHz and 0.2−0.3% spin population in the 3s orbital. The anisotropic part gives $T_\perp$ = 29.1−30.4 MHz, 28.9−30.1% spin in the 3p orbital, and a total of 29.1−30.4% spin population on the sulfur. Here we neglected the rhombicity of the hyperfine tensor. The QM/MM DFT calculation predicted a total Löwdin spin density on S of 36.3% (see Table S2 in the Supporting Information), most of which is in the 3p orbital and a negligible amount is on the 3s orbital (0.4%).[14] We tested the validity of our approach for calculating the spin population by calculating the spin population arising from the QM/MM DFT calculated values (see Table 4) and obtained 0.4% spin population in the 3s orbital and 37% on the p orbital. This yield a total spin population of 37.4%, which compares favorably with the QM/MM DFT value of 36.3%.

In Table 5 we compare the spin population we obtained from the ^{33}S hyperfine coupling and other values derived from other experimental parameters such as the β-proton hyperfine couplings and S K-pre-edge XAS data. Our results are in good agreement with those reported on the basis of ^{2}H

Table 5. Reported S Spin Density Values of Type I Azurin

method	sulfur spin population, %
[33]S hyperfine coupling	29.1−30.4
[2]H ENDOR[17]	30
S K pre-edge XAS[13]	45 (on the p orbital)
DFT[21]	62, 41 depending on the functional used (Mulliken)
QM/MM[20]	61
ab initio multireference determinantal configuration interaction (MRD-CI) calculations[22]	59.1
DFT[13]	28.7, 32.5[a] (C-squared population analysis, CSPA); 43.7, 36.9[a] (Mulliken population analysis)
QM/MM DFT calculations[14]	36.3 (Löwdin population)

[a]The two numbers correspond to calculations carried on a large model and a small model of azurin, which have been geometry optimized.

ENDOR of the cysteine β protons;[17] however, they are lower than the values derived from the XAS data.[13] The theoretical studies that reported a 62% spin density on the Sulfur atom[21,20,22] are highly overestimated in comparison with our data. Here we note that the spin populations obtained by the various analysis schemes, such as Mulliken and Löwdin population analysis, can yield different results for the same DFT calculations and therefore are best considered as qualitative[59] (see Table 5). They are useful for providing trends in calculations, provided that the same functional, basis set, and analysis scheme are used. This is in contrast to the direct calculation of the hyperfine interaction, which is unambiguous per a particular calculation.[59] Therefore, is better to compare the calculated and experimental hyperfine couplings (when available).

Considering that the total spin population should amount to 100% and that the spin population on the nitrogen ligand is ~10%[14] and on the β protons is 3%,[17] the 29−30.4% spin population on the thiolate leaves about 55% spin population on the Cu(II), which is higher than the reported value of 45%.[17] In this work, which reported an S spin population similar to ours and considering a somewhat overestimated spin population of 15% on the histidine nitrogens, the total spin population still did not reach 100%. Increasing the spin population on the S would mean increasing the A_z of the [33]S hyperfine coupling. We tried this, but it generated too large a discrepancy between the calculated and experimental 2D EDNMR spectra.

CONCLUSIONS

Using one- and two-dimensional EDNMR at W-band, we were able to detect the [33]S signals of type I Cu(II) in azurin. Whereas the orientation-selective 1D spectra showed a severe overlap with the ^{14}N signals of the coordinated nitrogens of His117 and His46, the 2D EDNMR spectra were dominated by [33]S signals. The [33]S hyperfine tensor was determined by simulations of the EDNMR spectra using QM/MM DFT predicted values as starting values, and to reach a reasonable agreement with the experimental spectra, the A_z value and one of the Euler angles had to be modified. This shows, once again, how important quantum chemical calculations are in providing the initial spin Hamiltonian values for data analysis in the absence of single crystals. Fitting 11 parameters without good initial values would be impossible. The final $(A_x, A_y, A_z) = (-27.0 \pm 1, -15.4 \pm 1, 67.5 \pm 2.5)$ MHz values gave a total S spin population of 29.8

± 0.7%, in comparison with values in the range of 29−62% reported in the literature, which were based on spectroscopic parameters and theoretical predictions.[13,14,17,20,21] Our direct experimental observation of the [33]S nuclear frequencies and the derived hyperfine coupling now provide an important constraint for further theoretical work in order to unravel the unique electronic properties of this site. Furthermore, with the new methodology we presented it will be possible to examine type I sites in different proteins and see if and how the [33]S hyperfine interaction and the associated spin population correlate with the redox potential and understand how it is tuned.

An interesting observation has been the small, but clearly detectable, difference in the hyperfine coupling of the coordinated ^{14}N of the histidine in a frozen solution and a frozen single crystal. This indicates that crystal forces do lead to some minor structural changes that affect the hyperfine coupling.

This work also demonstrates the effectiveness of 1D EDNMR and particularly 2D EDNMR for detecting nuclear transitions of low-γ quadrupolar nuclei. The new 2D EDNMR experiment requires further investigation in terms of optimization and resolution limitations. Finally, for the particular case of overlapping ^{14}N and [33]S signals, a higher EPR frequency would help in resolving them, as well as the use of ^{15}N-labeled protein.

ASSOCIATED CONTENT

Ⓢ Supporting Information

The Supporting Information is available free of charge on the ACS Publications website at DOI: 10.1021/acs.inorg-chem.7b00167.

Theory used for the simulations, additional parameters used for the simulations, QM/MM DFT orientation of the g, [33]S hyperfine. and quadrupole tensors orientations in the molecular frame, QM/MM DFT spin population distribution, X-band and W-band EDEPR simulations, and 1D and 2D EDNMR simulations (PDF)

AUTHOR INFORMATION

Corresponding Author
*E-mail for D.G.: Daniella.goldfarb@weizmann.ac.il.

ORCID Ⓘ
Yi Lu: 0000-0003-1221-6709
Daniella Goldfarb: 0000-0001-5714-7159

Notes
The authors declare no competing financial interest.

ACKNOWLEDGMENTS

■ REFERENCES

(1) Colman, P. M.; Freeman, H. C.; Guss, J. M.; Murata, M.; Norris, V. A.; Ramshaw, J. A. M.; Venkatappa, M. P. X-ray crysatl-structure analysis of plastocyanin at 2.7 A resolution. *Nature* **1978**, *272*, 319−324.

(2) Farver, O.; Pecht, I. Electron transfer in blue copper proteins. *Coord. Chem. Rev.* **2011**, *255*, 757−773.

(3) Gray, H. B.; Winkler, J. R. Electron flow through metalloproteins. *Biochim. Biophys. Acta, Bioenerg.* **2010**, *1797*, 1563−1572.

(4) Holwerda, R. A.; Wherland, S.; Gray, H. B. Electron-transfer reactions of copper proteins. *Annu. Rev. Biophys. Bioeng.* **1976**, *5*, 363−396.

(5) Nar, H.; Messerschmidt, A.; Huber, R.; Vandekamp, M.; Canters, G. W. Crystal-strcture analysis of oxidized Pseudomonas-Aeruginosa azirun at pH 5.5 and pH 9.0 -A pH-induced conformational transition involves a peptide-bond flip. *J. Mol. Biol.* **1991**, *221*, 765−772.

(6) Solomon, E. I. Spectroscopic methods in bioinorganic chemistry: Blue to green to red copper sites. *Inorg. Chem.* **2006**, *45*, 8012−8025.

(7) Coremans, J. W. A.; Poluektov, O. G.; Groenen, E. J. J.; Canters, G. W.; Nar, H.; Messerschmidt, A. A W-band Electron Nuclear Double Resonance study of single crystals of N-14 and N-15 azurin. *J. Am. Chem. Soc.* **1996**, *118*, 12141−12153.

(8) Malmstrom, B. G. Rack-induced bonding in blue-copper proteins. *Eur. J. Biochem.* **1994**, *223*, 711−8.

(9) Yanagisawa, S.; Banfield, M. J.; Dennison, C. The role of hydrogen bonding at the active site of a cupredoxin: The Phe114Pro azurin variant. *Biochemistry* **2006**, *45*, 8812−8822.

(10) Solomon, E. I.; Sundaram, U. M.; Machonkin, T. E. Multicopper oxidases and oxygenases. *Chem. Rev.* **1996**, *96*, 2563−2605.

(11) George, S. J.; Lowery, M. D.; Solomon, E. I.; Cramer, S. P. Copper L-edge spectra studies -A direct experimental probe of ground-state covalency in blue copper site in plastocyanin. *J. Am. Chem. Soc.* **1993**, *115*, 2968−2969.

(12) Shadle, S. E.; Pennerhahn, J. E.; Schugar, H. J.; Hedman, B.; Hodgson, K. O.; Solomon, E. I. X-ray absorption spectroscopic studsies of the blue copper site - metal and ligand K-edge studies to probe the origin of the EPR hyperfine splitting in plastocyanin. *J. Am. Chem. Soc.* **1993**, *115*, 767−776.

(13) Hadt, R. G.; Sun, N.; Marshall, N. M.; Hodgson, K. O.; Hedman, B.; Lu, Y.; Solomon, E. I. Spectroscopic and DFT studies of second-sphere variants of the type 1 copper site in azurin: covalent and nonlocal electrostatic contributions to reduction potentials. *J. Am. Chem. Soc.* **2012**, *134*, 16701−16.

(14) Lancaster, K. M.; Zaballa, M. E.; Sproules, S.; Sundararajan, M.; DeBeer, S.; Richards, J. H.; Vila, A. J.; Neese, F.; Gray, H. B. Outer-sphere contributions to the electronic structure of type zero copper proteins. *J. Am. Chem. Soc.* **2012**, *134*, 8241−53.

(15) Regan, J. J.; Dibilio, A. J.; Langen, R.; Skov, L. K.; Winkler, J. R.; Gray, H. B.; Onuchic, J. N. Electron-tunneling in azurin - the coupling across a beta-sheet. *Chem. Biol.* **1995**, *2*, 489−496.

(16) Gewirth, A. A.; Cohen, S. L.; Schugar, H. J.; Solomon, E. I. Spectroscopic and Theoretical-Studies of the Unusual Electron-Paramagnetic-Res Parameters of Distorted Tetrahedral Cupric Sites - Correlations to X-Ray Spectral Features of Core Levels. *Inorg. Chem.* **1987**, *26*, 1133−1146.

(17) Fittipaldi, M.; Warmerdam, G. C.; de Waal, E. C.; Canters, G. W.; Cavazzini, D.; Rossi, G. L.; Huber, M.; Groenen, E. J. Spin-density distribution in the copper site of azurin. *ChemPhysChem* **2006**, *7*, 1286−93.

(18) Kolczak, U.; Salgado, J.; Siegal, G.; Saraste, M.; Canters, G. W. Paramagnetic NMR studies of blue and purple copper proteins. *Biospectroscopy* **1999**, *5*, S19−S32.

(19) DeBeer, S.; Randall, D. W.; Nersissian, A. M.; Valentine, J. S.; Hedman, B.; Hodgson, K. O.; Solomon, E. I. X-ray absorption edge and EXAFS studies of the blue copper site in stellacyanin: Effects of axial amide coordination. *J. Phys. Chem. B* **2000**, *104*, 10814−10819.

(20) Moon, S.; Patchkovskii, S.; Salahub, D. R. QM/MM calculations of EPR hyperfine coupling constants in blue copper proteins. *J. Mol. Struct.: THEOCHEM* **2003**, *632*, 287−295.

(21) Remenyi, C.; Reviakine, R.; Kaupp, M. Density Functional Study of EPR Parameters and Spin-Density Distribution of Azurin and Other Blue Copper Proteins. *J. Phys. Chem. B* **2007**, *111*, 8290−8304.

(22) van Gastel, M.; Coremans, J. W. A.; Sommerdijk, H.; van Hemert, M. C.; Groenen, E. J. J. An ab initio quantum-chemical study of the blue-copper site of azurin. *J. Am. Chem. Soc.* **2002**, *124*, 2035−2041.

(23) Nar, H.; Messerschmidt, A.; Huber, R.; van de Kamp, M.; Canters, G. W. Crystal structure analysis of oxidized Pseudomonas aeruginosa azurin at pH 5.5 and pH 9.0. A pH-induced conformational transition involves a peptide bond flip. *J. Mol. Biol.* **1991**, *221*, 765−72.

(24) Finazzo, C.; Harmer, J.; Bauer, C.; Jaun, B.; Duin, E. C.; Mahlert, F.; Goenrich, M.; Thauer, R. K.; Van Doorslaer, S.; Schweiger, A. Coenzyme B induced coordination of coenzyme M via its thiol group to Ni(I) of F430 in active methyl-coenzyme M reductase. *J. Am. Chem. Soc.* **2003**, *125*, 4988−9.

(25) Astashkin, A. V.; Johnson-Winters, K.; Klein, E. L.; Byrne, R. S.; Hille, R.; Raitsimring, A. M.; Enemark, J. H. Direct demonstration of the presence of coordinated sulfate in the reaction pathway of Arabidopsis thaliana sulfite oxidase using ^{33}S labeling and ESEEM spectroscopy. *J. Am. Chem. Soc.* **2007**, *129*, 14800−10.

(26) Astashkin, A. V.; Johnson-Winters, K.; Klein, E. L.; Feng, C.; Wilson, H. L.; Rajagopalan, K. V.; Raitsimring, A. M.; Enemark, J. H. Structural studies of the molybdenum center of the pathogenic R160Q mutant of human sulfite oxidase by pulsed EPR spectroscopy and 17O and ^{33}S labeling. *J. Am. Chem. Soc.* **2008**, *130*, 8471−80.

(27) Enemark, J. H.; Raitsimring, A. M.; Astashkin, A. V.; Klein, E. L. Implications for the mechanism of sulfite oxidizing enzymes from pulsed EPR spectroscopy and DFT calculations for "difficult" nuclei. *Faraday Discuss.* **2011**, *148*, 249−67. Discussion 299−314.

(28) Schosseler, P.; Wacker, T.; Schweiger, A. Pulsed ELDOR detected NMR. *Chem. Phys. Lett.* **1994**, *224*, 319−324.

(29) Potapov, A.; Epel, B.; Goldfarb, D. A triple resonance hyperfine sublevel correlation experiment for assignment of electron-nuclear double resonance lines. *J. Chem. Phys.* **2008**, *128*, 052320.

(30) Florent, M.; Kaminker, I.; Nagarajan, V.; Goldfarb, D. Determination of the N-14 quadrupole coupling constant of nitroxide spin probes by W-band ELDOR-detected NMR. *J. Magn. Reson.* **2011**, *210*, 192−199.

(31) Potapov, A.; Lancaster, K. M.; Richards, J. H.; Gray, H. B.; Goldfarb, D. Spin Delocalization Over Type Zero Copper. *Inorg. Chem.* **2012**, *51*, 4066−4075.

(32) Un, S. Structure and Nature of Manganese(II) Imidazole Complexes in Frozen Aqueous Solutions. *Inorg. Chem.* **2013**, *52*, 3803−3813.

(33) Nagy, N. V.; Doorslaer, S. V.; Szabó-Plánka, T.; Rompaey, S. V.; Hamza, A.; Fülöp, F.; Tóth, G. K.; Rockenbauer, A. Copper(II)-Binding Ability of Stereoisomeric cis- and trans-2-Aminocyclohex-anecarboxylic Acid−l-Phenylalanine Dipeptides. A Combined CW/Pulsed EPR and DFT Study. *Inorg. Chem.* **2012**, *51*, 1386−1399.

(34) Aliabadi, A.; Zaripov, R.; Salikhov, K.; Voronkova, V.; Vavilova, E.; Abdulmalic, M. A.; Ruffer, T.; Buchner, B.; Kataev, V. Electron Spin Density on the N-Donor Atoms of Cu(II)-(Bis)oxamidato Complexes As Probed by a Pulse ELDOR Detected NMR. *J. Phys. Chem. B* **2015**, *119*, 13762−70.

(35) Kaminker, I.; Goldberg, H.; Neumann, R.; Goldfarb, D. High-Field Pulsed EPR Spectroscopy for the Speciation of the Reduced PV2Mo10O40 (6-) Polyoxometalate Catalyst Used in Electron-Transfer Oxidations. *Chem. - Eur. J.* **2010**, *16*, 10014−10020.

(36) Rapatskiy, L.; Cox, N.; Savitsky, A.; Ames, W. M.; Sander, J.; Nowaczyk, M. M.; Roegner, M.; Boussac, A.; Neese, F.; Messinger, J.; Lubitz, W. Detection of the Water-Binding Sites of the Oxygen-Evolving Complex of Photosystem II Using W-Band O-17 Electron-Electron Double Resonance-Detected NMR Spectroscopy. *J. Am. Chem. Soc.* **2012**, *134*, 16619−16634.

(37) Fittipaldi, M.; Garcia-Rubio, I.; Trandafir, F.; Gromov, I.; Schweiger, A.; Bouwen, A.; Van Doorslaer, S. A multi-frequency pulse EPR and ENDOR approach to study strongly coupled nuclei in frozen

solutions of high-spin ferric heme proteins. *J. Phys. Chem. B* **2008**, *112*, 3859−3870.

(38) Klein, E. L.; Raitsimring, A. M.; Astashkin, A. V.; Rajapakshe, A.; Johnson-Winters, K.; Arnold, A. R.; Potapov, A.; Goldfarb, D.; Enemark, J. H. Identity of the Exchangeable Sulfur-Containing Ligand at the Mo(V) Center of R160Q Human Sulfite Oxidase. *Inorg. Chem.* **2012**, *51*, 1408−1418.

(39) Cox, N.; Lubitz, W.; Savitsky, A. W-band ELDOR-detected NMR (EDNMR) spectroscopy as a versatile technique for the characterisation of transition metal-ligand interactions. *Mol. Phys.* **2013**, *111*, 2788−2808.

(40) Flores, M.; Agrawal, A. G.; van Gastel, M.; Gaertner, W.; Lubitz, W. Electron-electron double resonance-detected NMR to measure metal hyperfine interactions: Ni-61 in the Ni-B state of the NiFe hydrogenase of Desulfovibrio vulgaris Miyazaki F. *J. Am. Chem. Soc.* **2008**, *130*, 2402−2403.

(41) Kulik, L.; Epel, B.; Messinger, J.; Lubitz, W. Pulse EPR, Mn-55-ENDOR and ELDOR-detected NMR of the S-2-state of the oxygen evolving complex in Photosystem II. *Photosynth. Res.* **2005**, *84*, 347−353.

(42) Zamani, S.; Meynen, V.; Hanu, A.-M.; Mertens, M.; Popovici, E.; Van Doorslaer, S.; Cool, P. Direct spectroscopic detection of framework-incorporated vanadium in mesoporous silica materials. *Phys. Chem. Chem. Phys.* **2009**, *11*, 5823−5832.

(43) Banerjee, D.; Paniagua, J. C.; Mugnaini, V.; Veciana, J.; Feintuch, A.; Pons, M.; Goldfarb, D. Correlation of the EPR properties of perchlorotriphenylmethyl radicals and their efficiency as DNP polarizers. *Phys. Chem. Chem. Phys.* **2011**, *13*, 18626−18637.

(44) Bruch, E. M.; Warner, M. T.; Thomine, S.; Tabares, L. C.; Un, S. Pulse Electron Double Resonance Detected Multinuclear NMR Spectra of Distant and Low Sensitivity Nuclei and Its Application to the Structure of Mn(II) Centers in Organisms. *J. Phys. Chem. B* **2015**, *119*, 13515−23.

(45) Kaminker, I.; Wilson, T. D.; Savelieff, M. G.; Hovav, Y.; Zimmermann, H.; Lu, Y.; Goldfarb, D. Correlating nuclear frequencies by two-dimensional ELDOR-detected NMR spectroscopy. *J. Magn. Reson.* **2014**, *240*, 77−89.

(46) Kababya, S.; Nelson, J.; Calle, C.; Neese, F.; Goldfarb, D. Electronic structure of binuclear mixed valence copper azacryptates derived from integrated advanced EPR and DFT calculations. *J. Am. Chem. Soc.* **2006**, *128*, 2017−29.

(47) Radoul, M.; Sundararajan, M.; Potapov, A.; Riplinger, C.; Neese, F.; Goldfarb, D. Revisiting the nitrosyl complex of myoglobin by high-field pulse EPR spectroscopy and quantum mechanical calculations. *Phys. Chem. Chem. Phys.* **2010**, *12*, 7276−89.

(48) Marshall, N. M.; Garner, D. K.; Wilson, T. D.; Gao, Y.-G; Robinson, H.; Nilges, M. J.; Lu, Y. Rationally tuning the reduction potential of a single cupredoxin beyond the natural range. *Nature* **2009**, *462*, 113−116.

(49) Hosseinzadeh, P.; Marshall, N. M.; Chacon, K. N.; Yu, Y.; Nilges, M. J.; New, S. Y.; Blackburn, N. J.; Lu, Y. Design of a Single Protein that Spans the Entire 2V Range of Physiological Redox Potentials. *Proc. Natl. Acad. Sci. U. S. A.* **2016**, *113*, 262−267.

(50) Goldfarb, D.; Lipkin, Y.; Potapov, A.; Gorodetsky, Y.; Epel, B.; Raitsimring, A. M.; Radoul, M.; Kaminker, I. HYSCORE and DEER with an upgraded 95 GHz pulse EPR spectrometer. *J. Magn. Reson.* **2008**, *194*, 8−15.

(51) Mentink-Vigier, F.; Collauto, A.; Feintuch, A.; Kaminker, I.; Tarle, V.; Goldfarb, D. Increasing sensitivity of pulse EPR experiments using echo train detection schemes. *J. Magn. Reson.* **2013**, *236*, 117−125.

(52) Antholine, W. E.; Hanna, P. M.; McMillin, D. R. Low-frequency EPR of Pseudomonas-Aeruginosa azurin - analysis of ligand super-hyperfine structure from type-1 copper site. *Biophys. J.* **1993**, *64*, 267−272.

(53) Coremans, J. W. A.; Poluektov, O. G.; Groenen, E. J. J.; Canters, G. W.; Nar, H.; Messerschmidt, A. A W-band electron spin echo envelope modulation study of a single crystal of azurin. *J. Am. Chem. Soc.* **1997**, *119*, 4726−4731.

(54) Flanagan, H. L.; Singel, D. J. Analysis of 14N ESEEM patterns of randomly oriented solids. *J. Chem. Phys.* **1987**, *87*, 5606.

(55) Mims, W. B.; Peisach, J. The nuclear modulation effect in electron spin echoes for complexes of Cu2+ and imidazole with 14N and 15N. *J. Chem. Phys.* **1978**, *69*, 4921.

(56) Kofman, V.; Farver, O.; Pecht, I.; Goldfarb, D. Two-dimensional pulsed EPR spectroscopy of the copper protein azurin. *J. Am. Chem. Soc.* **1996**, *118*, 1201−1206.

(57) Coremans, J. W. A.; Poluektov, O. G.; Groenen, E. J. J.; Canters, G. W.; Nar, H.; Messerschmidt, A. W-band Elecron-paramagnetic-resonance study of single crystal of azurin. *J. Am. Chem. Soc.* **1994**, *116*, 3097−3101.

(58) Morton, J. R.; Preston, K. F. Atomic parameters for paramagnetic-resonance data. *J. Magn. Reson.* **1978**, *30*, 577−582.

(59) Neese, F. Quantum Chemistry and EPR Parameters. *eMagRes.* **2017**, *6*, 1.